



Evolution of the electrocatalytic activity of carbon-supported amorphous platinum–ruthenium–nickel–phosphorous nanoparticles for methanol oxidation

Yanjiao Ma^a, Hao Li^b, Hui Wang^a, Xuefeng Mao^a, Vladimir Linkov^c, Shan Ji^{c,1},
Okon Unathi Gcilitshana^c, Rongfang Wang^{a,*}

^a College of Chemistry and Chemical Engineering, Northwest Normal University, Lanzhou 730070, China

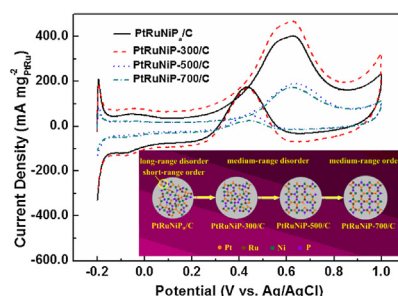
^b Department of Chemical Engineering, Huizhou University, Huizhou, Guangdong 516007, China

^c South African Institute for Advanced Materials Chemistry, University of the Western Cape, Private Bag X17, Bellville, Cape Town 7535, South Africa

HIGHLIGHTS

- Amorphous PtRuNiP/C catalyst with different disorder degree was prepared.
- Amorphous PtRuNiP-300/C catalyst showed high activity for methanol oxidation.
- The correlation between amorphous structure and their activity was established.

GRAPHICAL ABSTRACT



ARTICLE INFO

Article history:

Received 25 February 2014

Received in revised form

4 June 2014

Accepted 17 June 2014

Available online 25 June 2014

Keywords:

Nanoparticles

Amorphous

Crystallinity

Electrocatalyst

Methanol oxidation

ABSTRACT

Amorphous metallic nanoparticles hold much promise for use as electrocatalysts, as their surface is rich in low-coordination sites and defects which could act as the electrocatalyst's active sites. In this study, we describe new findings on amorphous platinum–ruthenium–nickel–phosphorous nanoparticles supported on carbon (PtRuNiP_a/C) and the comparison between their catalytic activity and the degree of disorder. The nanoscale amorphous structure with different degrees of disorder are probed as a function of surface composition, particle size, and thermal treatment conditions using X-ray diffraction, X-ray photoelectron spectroscopy, transmission electron microscopy, selected area electron diffraction and electrochemical characterization. The results provide experimental evidence in support of nanoscale long-range disorder, medium-range disorder, and medium-range order evolution dependence on the catalyst synthesis temperature. More importantly, the results of the electrochemical performance investigation show that the amorphous structures with medium-range disorder have not only better catalytic activity, but also better durability for methanol oxidation compared to the long-range disorder and medium-range order structure. These results provide an opportunity for establishing the correlation between the nanoscale amorphous structure and their electrocatalytic activity for methanol oxidation reaction, which could play an important role in developing new high active catalysts for direct methanol fuel cells.

© 2014 Elsevier B.V. All rights reserved.

* Corresponding author. Tel./fax: +86 931 7971533.

E-mail addresses: sji@uwc.ac.za (S. Ji), wrf38745779@126.com, wangrf@nwnu.edu.cn (R. Wang).

¹ Tel./fax: +27 21 9599316.

1. Introduction

PtRu bimetallic electrocatalysts are considered as promising electrocatalysts for direct methanol fuel cells (DMFC) due to their high catalytic activity and CO tolerance [1]. In spite of making extensive efforts to optimize the structure and morphology of PtRu bimetallic catalysts to further improve their performance and, activity, their cost is still too high to meet the requirements for practical applications [2].

It is well demonstrated that the electrocatalytic characteristics such as activity, selectivity, and stability rely heavily on the surface atomic arrangement and configurations associated with terraces, steps, kinks and vacancies [3,4]. During the past decades, surface scientists have systematically studied the catalytic surface/structure correlations using metal single-crystal planes as model catalysts and found that the surfaces with an open structure (e.g. the high-index planes, denoted by a set of Miller indices (*hkl*) with at least one index being larger than unit) usually exhibit much high activity and stability [5,6]. High catalytic activity results from the high-index plane surfaces with high density of atomic steps and kinks, where low-coordinated atoms can easily interact with reactant molecules and serve as active sites for breaking chemical bonds [7]. Pt-based nanoparticles with high-index facets have been developed to meet the requirement of anode catalyst in DMFC [8]. Unfortunately, it is rather challenging to synthesize either high-index planes of bulk metals or Pt-based nanoparticles enclosed by high-index facets.

Amorphous alloys are a kind of metastable materials with long-range disordered but short-range ordered structure [9], which enable amorphous alloys to form a plenty of low-coordination sites (terraces, steps, corner atoms) and defects on the surface [10,11]. It is well-documented that low-coordination sites play important roles in catalysis. Ni and Co-based amorphous alloys have been employed as catalysts in many hydrogenation reactions [12,13]. Due to their superior corrosion resistance, amorphous alloys show very good stability during the catalysis process [10,11].

In the field of electrochemical catalysis, only a few studies have been reported on the amorphous electrocatalysts. For instance, Ni_3NbPt -based amorphous electrocatalysts prepared by ball milling showed good electrocatalytic activity for small organic molecule oxidation [14]. PtRu-based amorphous electrocatalysts synthesized by chemical methods for small organic molecule oxidation were rarely explored. Therefore, it is an interesting work to develop amorphous structured PtRu-based catalysts with enhanced activity and stability.

Phosphorus, an inexpensive metalloid element, has several valence electrons. Some studies found that P element can enhance the electrocatalytic activity for small organic molecule oxidation [15–18]. Incorporating P into noble metal electrocatalysts has the following merits: (i) particle size reduction, which increases the amount of active sites [18,19]; (ii) reduction of particle agglomeration during the long-term operation of the fuel cell, leading to the good stability of electrocatalysts [18]; (iii) changes on the electronic states of the metal elements, resulting in the enhanced amount of Pt^0 formed in the electrocatalysts [20]. Moreover, it was proven that the small nanoparticle size of the crystalline PtRuNiP catalyst enhanced its catalytic activity for methanol oxidation [21].

Based on the above considerations, we synthesized PtRuNiP nanoparticles with an amorphous structure (denoted as PtRuNiP_a/C) highly dispersed on the carbon surface, and investigated its catalytic activity towards methanol oxidation reactions. Moreover, the nanoparticles with various degrees of crystallinity, e.g. various degrees of disorder [22], were also prepared by heat-treatment at the appropriate temperature and their electrochemical performances were also systematically investigated. Comparison of the

results showed that the amorphous PtRuNiP electrocatalyst after heat-treatment at 300 °C exhibited the highest electrocatalytic activity and durability.

2. Experimental

2.1. Preparation of PtRuNiP/C catalysts with different degrees of crystallinity

Amorphous PtRuNiP/C catalyst was prepared by a NaBH_4 reduction reaction in an aqueous solution. The detailed preparation process could be described as follows: 475 mg of $\text{NiCl}_2 \cdot 6\text{H}_2\text{O}$, and 318 mg of $\text{NaH}_2\text{PO}_2 \cdot \text{H}_2\text{O}$ were dissolved in aqueous solutions and stirred for 0.5 h. The pH of the system was adjusted to ~7.5 by the drop wise addition of a 6 mol L^{-1} NaOH solution with vigorous stirring. And then 3.41 mL of 20 mg mL^{-1} H_2PtCl_6 and 1.76 mL of 20 mg mL^{-1} RuCl_3 was rapidly added to the solution and with continuous stirring for another 0.5 h. Pretreated carbon black Vulcan® XC72R (250 mg) was added to the mixture under stirring conditions. Afterward, 20 mL of 0.2 mol L^{-1} NaBH_4 aqueous solution was added slowly to the mixture to react for 12 h. The product (PtRuNiP/C) was collected by filtration, washed with 6 mol L^{-1} ammonia solution, then with deionized water several times and kept in ethanol solution.

The product was then thermally treated in a tube furnace under N_2 atmosphere at 300, 500, and 700 °C for 2 h, respectively. The obtained products were then denoted as PtRuNiP-300/C, PtRuNiP-500/C, and PtRuNiP-700/C, respectively. For comparison, PtRu/C catalyst was prepared using the same procedure but the absence of the precursor of Ni and P.

2.2. Physical characterization

The catalysts were characterized by recording their X-ray diffraction (XRD) patterns on a Rigaku D/Max-2400 (Japan), using filtered Cu-K_α radiation ($\lambda = 0.15418$ nm), generated at 50 kV and 150 mA. Scans for 2θ values were recorded at 4° min^{-1} between 10 and 90° . Transmission electron micrographs (TEM), high angle annular dark field scanning transmission electron microscopy (STEM) images and selected area electron diffraction (SAED) patterns of the catalysts were taken on a JEOL (JEM-2000 FX) microscope operating at 200 kV. Energy dispersive spectroscopy (EDS) in the STEM mode was employed for determining elemental composition of either individual particle or several particles. The crystallization behavior study was performed with a diffractometer scanning calorimetry (DSC) instrument system (Mettler Toledo) at a scan rate of $20^\circ \text{ C min}^{-1}$ up to 800 °C under N_2 atmosphere. X-ray photoelectron spectra (XPS) were acquired with a VG Escalab 210 spectrometer fitted with a Mg 300 W X-ray source.

2.3. Electrochemical measurements

The electrochemical measurements of the catalysts were performed using the electrochemical work station CHI 650D. A common three-electrode electrochemical cell was used for the measurements. The counter and reference electrodes were a platinum wire and an Ag/AgCl (3 mol L^{-1} KCl) electrode, respectively. The working electrode was a glassy carbon disk (5 mm in diameter). The thin-film electrode was prepared as follows: 5 mg of catalyst was dispersed ultrasonically in 1 mL Nafion/ethanol (0.25% Nafion) solution for 15 min. 8 μL of the dispersion was transferred onto the glassy carbon disk using a pipette, and then dried in the air. The stable cyclic voltammograms (CVs) were recorded after 24 cycles. All potentials initially measured versus the Ag/AgCl electrode were

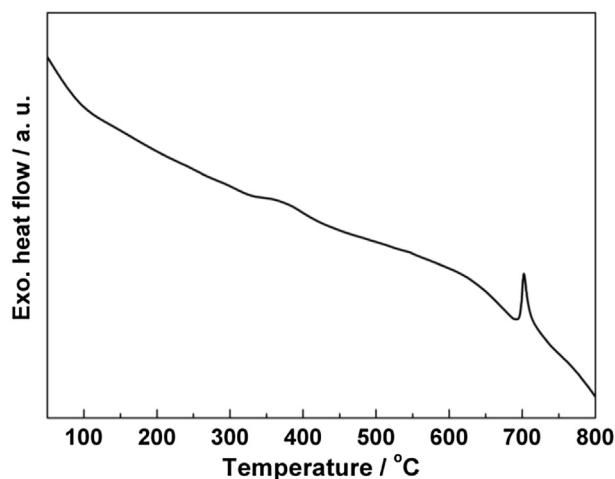


Fig. 1. Continuous heating DSC curves of PtRuNiP_a sample at a heating rate of 10 °C min⁻¹.

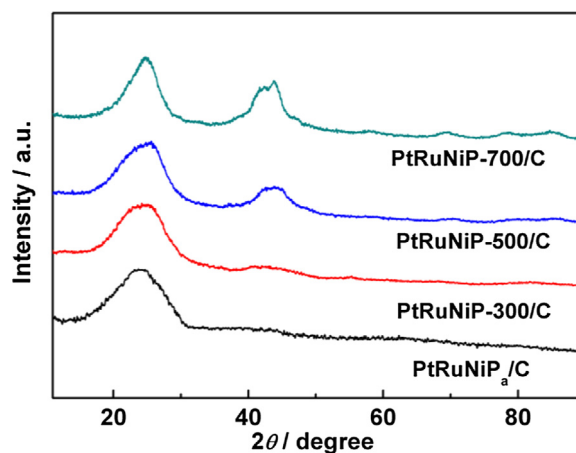


Fig. 2. The XRD patterns of the PtRuNiP/C catalysts.

converted to a RHE scale by adding 0.197 V (the potential of the Ag/AgCl reference measured against RHE).

3. Results and discussion

The optimization of the heat-treatment temperature of the amorphous PtRuNiP_a/C to obtain the appropriate structure was the first goal of the study. Here, DSC measurement (see Fig. 1) was used to study the crystallization behavior of the amorphous PtRuNiP_a/C. Considering the presence of carbon support which may make the data analysis difficult, un-supported sample was prepared for using in DSC measurement. One weak exothermic peak at around 700 °C can be observed in Fig. 1, which indicates that the phase transformation and crystallization of PtRuNiP_a nanoparticles occurred at this temperature [12,23,24]. On the other hand, it was reported that the surface segregation of PtRu alloy also occurs at the temperature range from ca. 200–500 °C under different atmospheres [25–27]. Thus, the amorphous PtRuNiP_a/C catalyst was heat treated at three temperatures i.e. 300, 500 and 700 °C, respectively, and the products were further studied. These products were denoted as PtRuNiP-300/C, PtRuNiP-500/C, and PtRuNiP-700/C, respectively.

The XRD patterns of all the prepared catalysts are presented in Fig. 2. All catalysts show a diffraction peak at about 24°, which corresponds to the (200) reflection of the hexagonal structure of Vulcan carbon. For the PtRuNiP_a/C catalyst, no clear peak can be observed, suggesting that the structure of PtRuNiP_a nanoparticles is amorphous and/or the crystallite size is very small [28–30]. For PtRuNiP-300/C catalyst, a weak broad peak within a wide 2θ range (36–49°) was observed, without any trace of sharp peaks related to the periodic lattice, which suggests that the PtRuNiP-300/C catalyst's structure is still amorphous. The relative strong intensity of a broad peak at ca. 43° was observed after the catalyst was heat-treated at 500 °C. This is a result of annihilation of point defects and dislocation [31,32] or partial crystallization [33]. After heat-treatment of the product at 700 °C, the XRD spectrum showed two new peaks at around 40 and 43°, which corresponds to the (110) plane of crystalline Pt alloy and (112) reflection of crystalline Ni₃P phase (JCPDS card No. 34-0501), indicating that the phase-separated and the nanocrystalline structure is formed at around 700 °C [34,35].

Another technique used to give further information on structural changes is SAED patterns, which is shown as Fig. 3. A

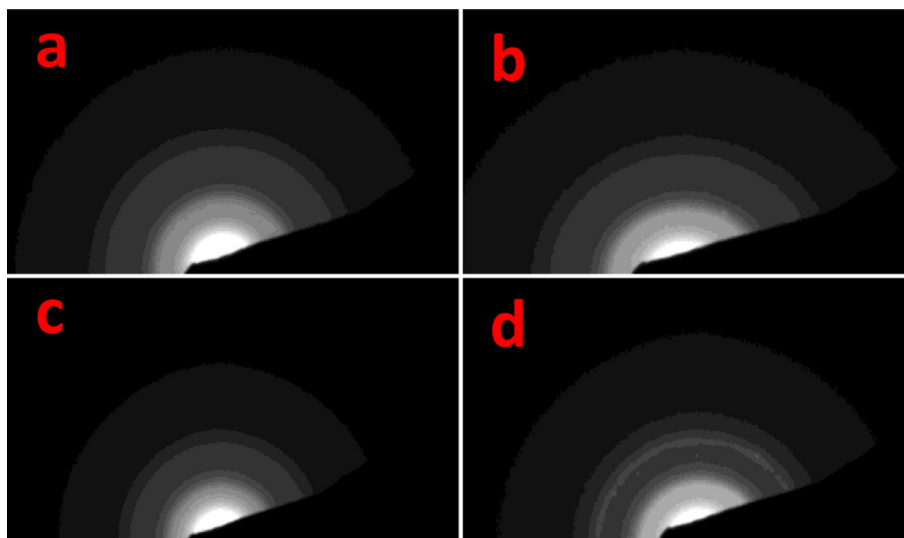


Fig. 3. The SAED patterns of the PtRuNiP_a/C (a), PtRuNiP-300/C (b), PtRuNiP-500/C (c) and PtRuNiP-700/C (d) catalysts.

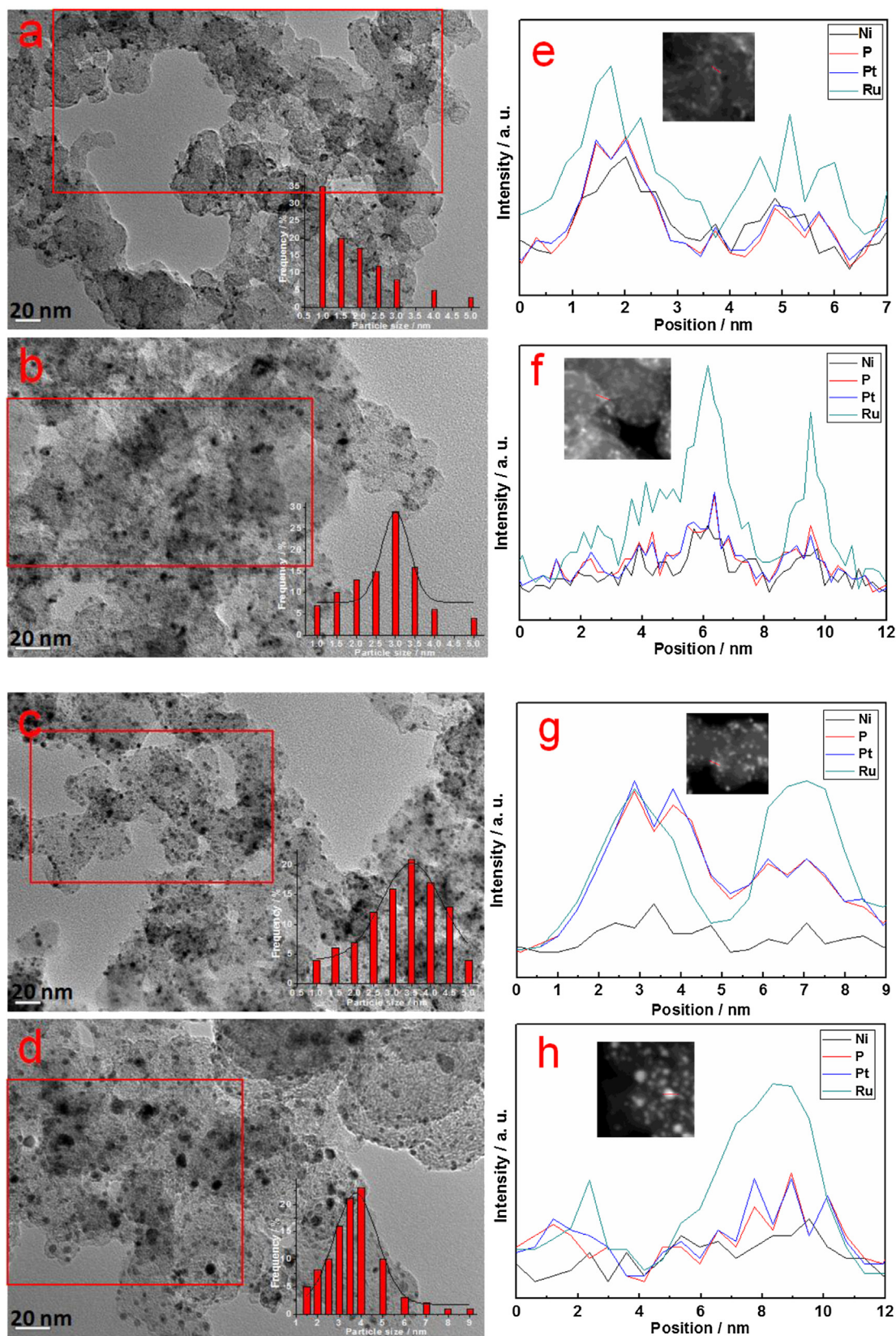


Fig. 4. TEM images and the line-scan EDX profiles; the insets are the corresponding histogram of PtRuNiP particle size distribution in a-d and the STEM images in e-h, of the PtRuNiP₄/C (a and e), PtRuNiP-300/C (b and f), PtRuNiP-500/C (c and g), and PtRuNiP-700/C (d and h) catalysts, respectively; The scale of red line in STEM images is consistent with that of horizontal axis of the line-scan EDX profiles. (For interpretation of the references to color in this figure legend, the reader is referred to the web version of this article.)

continuous hollow ring, which is a typical diffraction pattern of an amorphous material, can be observed in Fig. 3a, confirming the amorphous structure of PtRuNiP_a/C [36]. For the SAED patterns of the products heat treated at 300 and 500 °C (Fig. 3b and c), no change was observed when compared to that of PtRuNiP_a/C, indicating that the structure was still amorphous. However, for the 700 °C heat treated catalyst, some Laue spots were observed (Fig. 3d) indicating that the crystalline structure was formed [37]. The SAED results confirmed the results of the XRD and DSC.

Fig. 4a–d provides TEM images of the four catalysts and the corresponding rough histogram of the particle size distributions obtained by measuring about 100 randomly selected particles in the red box. Fig. 4e–h shows the line-scan EDS profiles and the corresponding STEM images (the insets). From Fig. 4a, it is evident that the PtRuNiP_a nanoparticles are evenly distributed on the carbon surface, and the nanoparticle size distribution ranges from ~1.0–5.0 nm with the average particle size of ca. 1.8 nm. The composition of PtRuNiP_a/C was analyzed by EDS and results are shown in Fig. S1 (Supporting information). The quantitative elemental analysis shows that the Pt:Ru:Ni:P atomic ratio is nearly 1.0:1.6:2.6:3.0, and the loading of PtRuNiP nanoparticles is ca. 19.8 wt%, which is obviously lower than the normal loading, implying that the metal precursors were partially reduced. The distribution profile of the elements is shown in Fig. 4e, in which the corresponding STEM images are presented. It can be seen that Pt manifests itself in two peaks, and the same is observed for all the other elements. The positions and widths of the peaks of all the elements match well with each other, showing that the four elements were evenly distributed in the PtRuNiP_a nanoparticles.

In the TEM image of PtRuNiP-300/C, which is presented in Fig. 4b, the PtRuNiP-300 nanoparticles have a uniform and narrow size distribution with an average diameter of 3.0 nm. From this, it is evident that the heat-treatment at 300 °C induces agglomeration, which results in the increase in particle size. However, the distribution profile of the elements presented in Fig. 4f shows that the Ni, P, Ru and Pt elements are evenly distributed in the PtRuNiP-300 nanoparticles. Similarly, with PtRuNiP-500/C (Fig. 4c) and PtRuNiP-700/C (Fig. 4d and h), nanoparticles are also uniformly dispersed with an average particle size of 3.5 nm and 3.7 nm, respectively, with the distribution of the four elements also similar to that of the PtRuNiP_a and PtRuNiP-300 nanoparticles (Fig. 4e).

As shown in Fig. 5, the range of the nanoparticle size broaden, and the average particle size increases as the temperature of heat-treatment increases from 300 to 700 °C. On the other hand, the uniform distribution of the Pt, Ru, Ni and P elements from

PtRuNiP_a/C to PtRuNiP-700/C indicates that the alloy structure did not change with the heat treatment temperatures.

XPS analysis was carried out to determine the surface composition and the valence state of the catalysts. The XPS survey spectra of the all catalysts are shown in Supporting information, Fig. S2, in which O 1s, C 1s, P 2p, Ru 3p, Pt 4f, and Ni 2p signals were detected. By calculating the peak areas of elemental Pt, Ru, Ni, and P, the surface compositions of the four catalysts are provided in Table 1. The content of Ru, Ni and P follows a volcano curve trend compared to that of Pt, i.e. initially the content increases from PtRuNiP_a/C to PtRuNiP-500/C and then decreases. By investigating the composition change of PtRu/C catalyst, Wang's group [25,38,39] found that the process of Ru surface segregation driven by atmospheric attraction competes with the Pt surface segregation driven by the surface energy. Thus, the surface segregations induced by the surface energy and the atmospheric attraction lead to the composition change on the surface of PtRuNiP nanoparticles.

The Pt 4f XPS of the four catalysts are shown in Fig. 6. The spectrum can be fitted into three pairs of doublets in all catalysts. The highest intense doublet is the Pt(0) peaks of metallic state, the middle one is the oxidation state Pt(II) in PtO and Pt(OH)₂-like species, and the lowest one can be assigned to a higher oxidation state Pt(IV) [40,41]. The fitting results of the Pt 4f_{7/2} component are listed in Table 1. It can be observed that Pt in all the catalysts is predominately presented in the zero valent metallic state, and the

Table 1

Assignments, binding energies (BEs) and concentrations of Pt 4f species in various catalysts obtained from XPS results.

Catalyst	Pt:Ru:Ni:P ^a	Pt 4f _{7/2}	BE ^b	Concentration ^c
PtRuNiP _a /C	1.0:2.5:2.1:2.5	Pt(0)	71.9	0.25
		Pt(II)	72.7	0.45
		Pt(IV)	74.4	0.30
PtRuNiP-300/C	1.0:3.4:1.8:2.7	Pt(0)	71.9	0.16
		Pt(II)	72.8	0.55
		Pt(IV)	74.5	0.29
PtRuNiP-500/C	1.0:4.5:2.5:2.7	Pt(0)	71.9	0.27
		Pt(II)	72.5	0.46
		Pt(IV)	74.4	0.27
PtRuNiP-700/C	1.0:3.4:2.3:1.7	Pt(0)	71.7	0.28
		Pt(II)	72.3	0.51
		Pt(IV)	74.4	0.21

^a Atomic ratio.

^b Binding energy (in eV).

^c Per species (in at %).

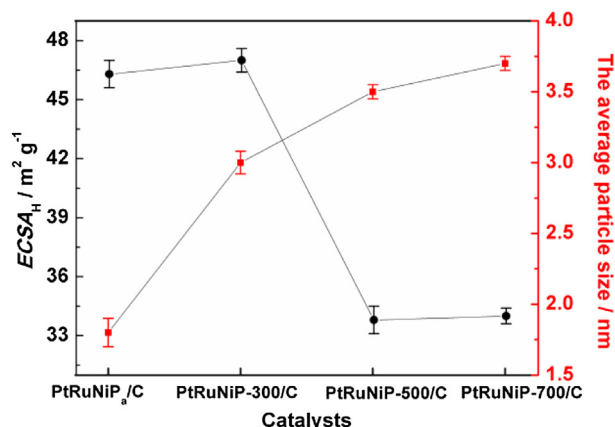


Fig. 5. The changes of the ECSA and average particle size of the four catalysts.

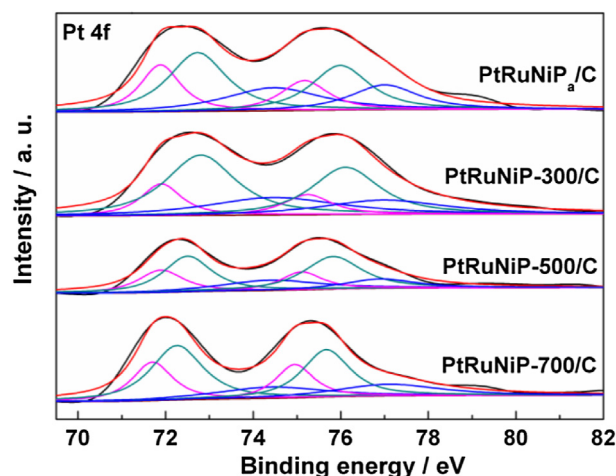


Fig. 6. The Pt 4f XPS spectra of the four catalysts.

content of Pt(0) relative to the total quantity of Pt does not significantly change from PtRuNiP_a/C to PtRuNiP-700/C.

However, it is obvious that the binding energies of Pt 4f show negative shifts from PtRuNiP_a/C to PtRuNiP-700/C. The correlation of the shifts of the Pt 4f XPS binding energies with the electronic can provide important information about the relationship between their structural and electrochemical properties. It has been extensively studied by some groups [42–44] that the reduction of the metal particle size leads to the positive shift of binding energies. In the case of PtRuNiP/C catalysts, the negative shifts of binding energies from PtRuNiP-300/C to PtRuNiP-700/C are also the result of the particle sizes effect. However, the particle size effect cannot explain the positive shifts of Pt 4f binding energy of PtRuNiP-300/C and PtRuNiP_a/C.

Based on the combined experimental and theoretical analysis of the shift, Richter et al. proposed that the origin of the initial or final state effects is connected to the lattice strain, and that the binding energy shift is related to the degree of hybridization being larger for shorter bond distances [45]. It should be noted that the above conclusions were obtained on the basis of the constant structure of the investigated particles. As previously discussed, the structure of PtRuNiP nanoparticles changed from nanoscale amorphous to partially crystalline phase when the heat treatment temperature was increased. During the process, annihilation of point defects and dislocation within the grains and grain boundary zones occurred along with rearrangement of atoms, which led to the change of the chemical bonding between Pt atoms with other atoms, and further resulted in the shift of binding energy. Besides, from PtRuNiP_a/C to PtRuNiP-700/C, the shifts of binding energy do not vary monotonically with the particle size because the structure of the particles also changes. In particular, the highest binding energy shift of Pt 4f XPS in PtRuNiP_a/C refers to the downshift of the center of the d-band in respect to the Fermi level, which would lead to the decrease in the bond strength of adsorbents towards small molecule formed during the oxidation of methanol [46,47].

In the case of ruthenium, the Ru 3p signal can be deconvoluted into three distinguishable doublets with different intensities for PtRuNiP_a/C and PtRuNiP-300/C, and two doublets for PtRuNiP-500/C and PtRuNiP-700/C (Fig. 7 and Table 2). The peak at 461.9–462.5 eV is attributed to metallic Ru (Ru(0)), while the two peaks at 463.9–464.1 and 466.2 eV in all catalysts are assigned to anhydrous RuO₂ and hydrous amorphous RuO_xH_y [1,40]. The absence of RuO₂·xH₂O in PtRuNiP-500/C and PtRuNiP-700/C is as a result dehydration of RuO_xH_y with heat-treatment at elevated temperature. As shown in Table 2, Ru in PtRuNiP_a/C and PtRuNiP-300/C is predominately presented in the oxidation state, while

Table 2

Assignments, binding energies (BEs) and concentrations of Ru 3p species in various catalysts obtained from XPS results.

Catalyst	Ru 3p	BE ^a	Concentration ^b
PtRuNiP _a /C	Ru	462.5	0.18
	RuO ₂	464.1	0.64
	RuO _x H _y	466.2	0.18
PtRuNiP-300/C	Ru	462.2	0.09
	RuO ₂	464.1	0.74
	RuO _x H _y	466.2	0.17
PtRuNiP-500/C	Ru	461.9	0.84
	RuO ₂	463.9	0.16
	RuO _x H _y	—	—
PtRuNiP-700/C	Ru	462.1	0.84
	RuO ₂	463.9	0.16
	RuO _x H _y	—	—

^a Binding energy (in eV).

^b Per species (in at %).

most of Ru in PtRuNiP-500/C and PtRuNiP-700/C is in metallic state, which would influence the catalytic activity. In addition, the shifts of binding energy of Ru 3p can be clearly observed, and the trend is similar to that of Pt 4f binding energy. The result implies that the chemical bonding between Ru and the other atoms changes with the heat treatment temperature. The XPS spectra of Ni 2p and P 2p are presented in Figs. S3–S4 and Table S1–S2 in Supporting information.

A diagram shown in Fig. 8 illustrates the evolution of the surface and composition of PtRuNiP nanoparticles. The main structural feature of PtRuNiP_a nanoparticles is a long-range disorder accompanied by a short-range order [32]. After the heat treatment, the amorphous phase is still retained, but annihilation of point defects and dislocation within the grains and grain boundary zones led to the medium-range disorder, i.e. the order range becomes longer [31], which is complemented by the rearrangement of atoms. Similar change of order range has been observed by Carlo and Alfredo in amorphous GeSe₂ [22]. When the heat treatment temperature increased, the order range became long, as shown in the structure of PtRuNiP-300/C and PtRuNiP-500/C. The phase transitioned from amorphous to crystalline phase occurs once the temperature was elevated to 700 °C where the exothermic peak appears. The medium-range order is formed in PtRuNiP-700/C.

Cyclic voltammograms (CVs) measured in a nitrogen-saturated 0.5 mol L^{−1} H₂SO₄ solutions are shown in Fig. 9. All catalysts clearly exhibit the characteristic features of PtRu catalysts supported on carbon. It can be observed on the forward section of the first scan that there is a hydrogen desorption peaks in the low potential region (−0.03 to 0.297 V), and a peak at higher potential, between 0.797 V and 1.197 V corresponding to the oxidation of metal [48]. On the reverse scan, the peak at 0.737 to 0.567 V is the characteristic of metal oxide reduction and a hydrogen adsorption peak appears at low potential range [49]. The difference between these four catalysts is the capacitive current in the double-layer region. The capacitive current follows the order: PtRuNiP-300/C > PtRuNiP_a/C > PtRuNiP-500/C ≈ PtRuNiP-700/C. The obtained capacitive current increases with the RuO₂ content. This capacitive current in the double-layer region is ascribed to the adsorption of oxygen-containing species (probably OH) on the Ru atoms, which plays an important role in the electrooxidation of methanol [50,51].

The electrochemical surface area (ECSA) is an important factor for the fuel cell reactions and the utilization ratio of electrocatalyst is closely connected with the ECSA. The ECSA values of the prepared catalysts were calculated according to the equation [51,52]:

$$\text{ECSA} = Q_{\text{H}} / (2.1\omega) \quad (1)$$

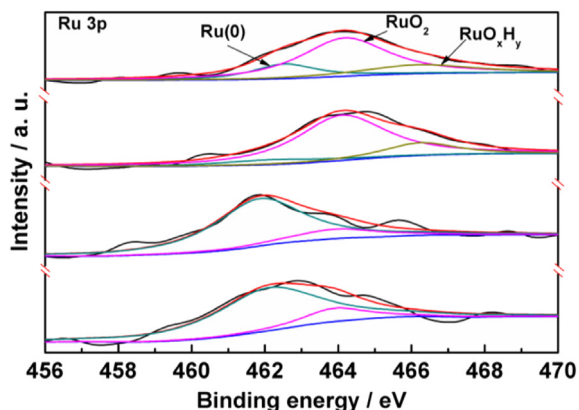


Fig. 7. The Ru 3p XPS spectra of the four catalysts.

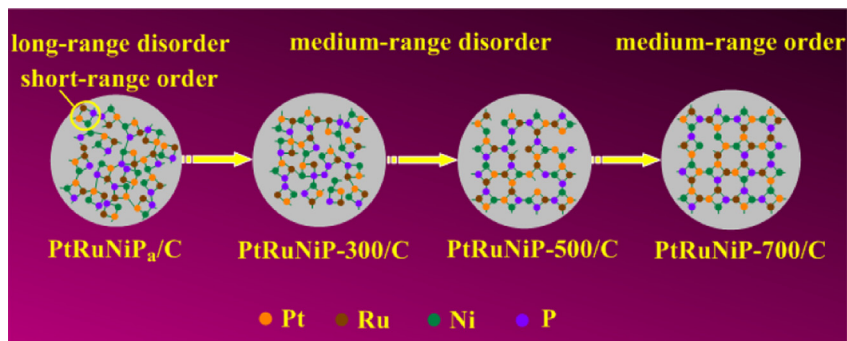


Fig. 8. Schematic illustration evolution of the structure of PtRuNiP nanoparticles.

where Q_H ($C m^{-2}$) is the average integrated charge in the hydrogen adsorption and desorption peak (-0.03 to 0.297 V) area of the CV curves after subtracting the contribution from the double-layer region, ω is the Pt loading on the electrode, and 2.1 is the charge ($C m^{-2}$) required to oxidize a monolayer of hydrogen on the precious metal surface, respectively. The values of ECSA are listed in Fig. 5, and it can be seen that the values of ECSA follow the order: $PtRuNiP_a/C \approx PtRuNiP-300/C > PtRuNiP-500/C \approx PtRuNiP-700/C$. The PtRuNiP nanoparticles with amorphous structure have the largest ECSA value among all the prepared catalysts.

The electrocatalytic activities of the four prepared PtRuNiP/C catalysts towards methanol oxidation are shown in Fig. 10. For comparison, the activity of as-prepared PtRu/C was also displayed in the figure. The currents were normalized to the Pt + Ru loading and ECSA, corresponding to the mass activity and specific activity

respectively. Onset potential and the current of methanol oxidation at fixed potential were adopted to study of the catalytic activity for these four PtRuNiP/C catalysts, and the results are listed in Table 3. It can be observed that the onset potential of methanol oxidation on PtRu/C electrode is higher than those of the four PtRuNiP/C catalysts, suggesting that the presence of Ni and P can deduce the onset potential of methanol oxidation on PtRu particles. As shown in Table 3, the catalytic activities of these four catalysts follow the order: $PtRuNiP-300/C > PtRuNiP_a/C > PtRuNiP-500/C > PtRuNiP-700/C$. The trend of the activity of four PtRuNiP/C catalysts is consistent with the values of ECSA. In addition, the catalytic activity of PtRu/C is in the middle in terms of the mass activity and specific activity, suggesting the appropriate dispersion of PtRuNiP nanoparticles can enhance the catalytic activity.

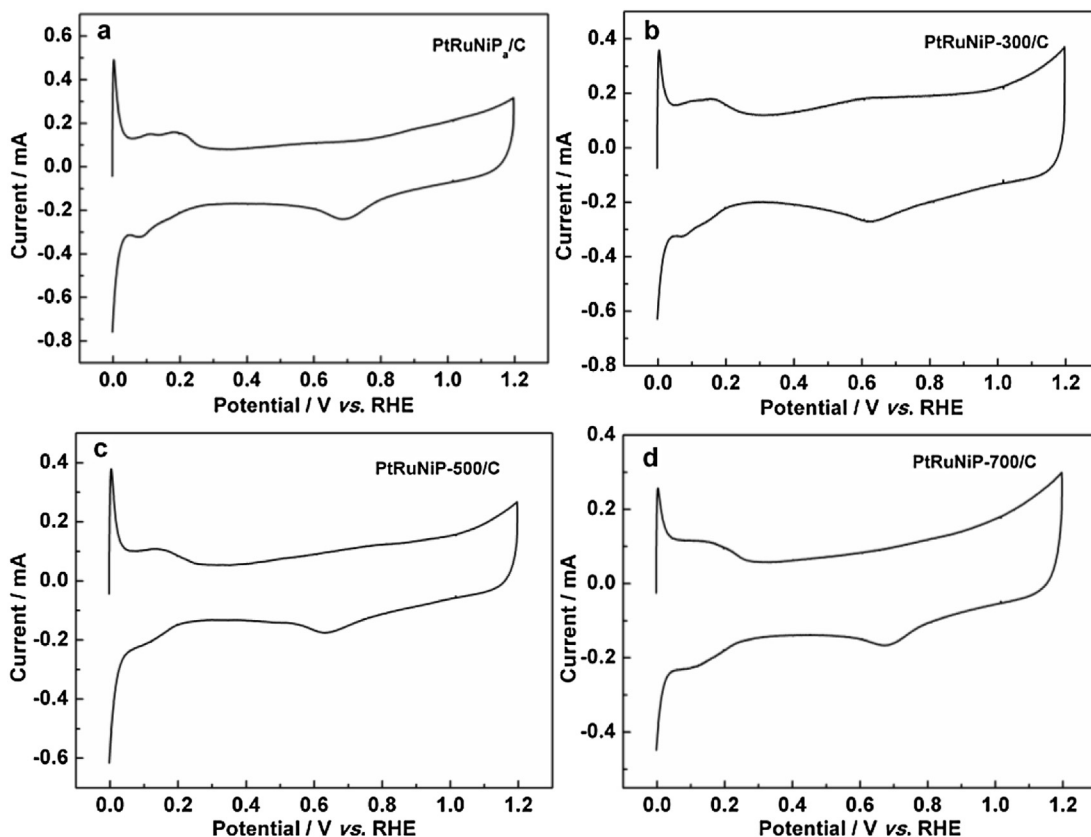


Fig. 9. CVs of the four PtRuNiP catalysts at N_2 -saturated $0.5 \text{ mol L}^{-1} H_2SO_4$ solution with 50 mV s^{-1} of a scan rate.

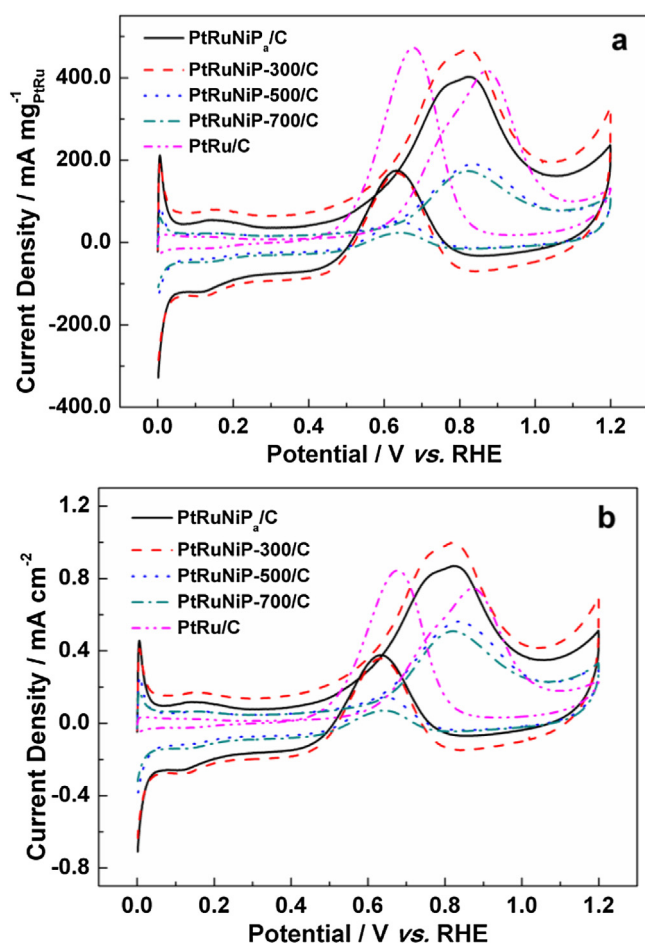


Fig. 10. CVs of the all catalysts in 0.5 mol L⁻¹ CH₃OH + 0.5 mol L⁻¹ H₂SO₄ at 50 mV s⁻¹; (a) and (b) are normalized by the Pt + Ru loading and ECSA_H, respectively.

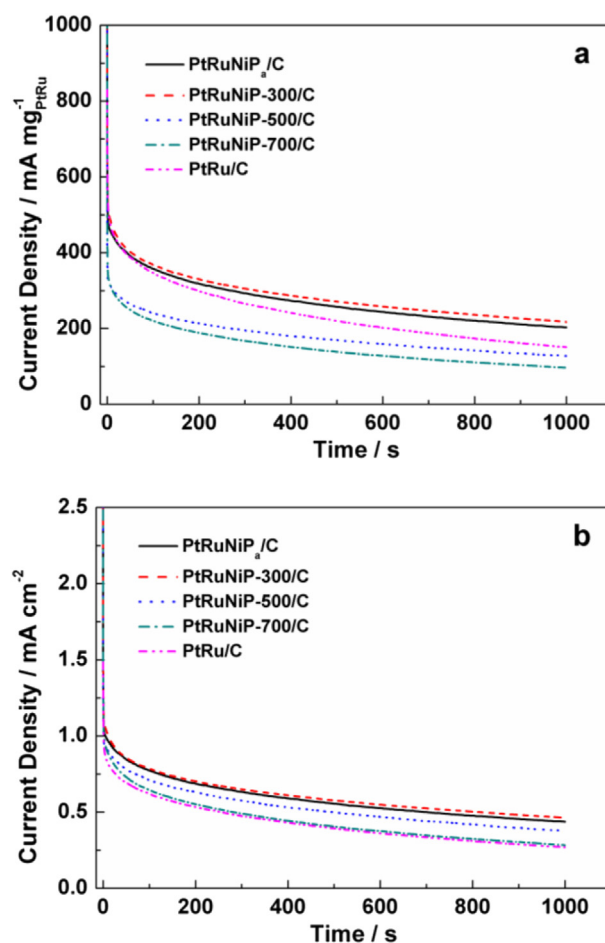


Fig. 11. Chronoamperometry curves normalized by the Pt + Ru loading and ECSA_H of the all catalysts in 0.5 mol L⁻¹ CH₃OH + 0.5 mol L⁻¹ H₂SO₄ at fixed 0.797 V, respectively.

Fig. 11 shows the chronoamperometric curves of the catalysts measured in 0.5 mol L⁻¹ H₂SO₄ and 0.5 mol L⁻¹ CH₃OH at a constant potential of 0.797 V. For all catalysts, the potentiostatic current decreases rapidly in the initial period of time which can be due to the formation of CO_{ads} and other intermediate species during the methanol oxidation reaction. The current density gradually decayed and a pseudo-steady state was achieved over time; this decay can be attributed to the adsorbed anion and intermediate present on the catalyst surface, restricting the methanol oxidation reaction [53]. The results demonstrate that the durability of these four catalysts follows the following order: PtRuNiP-300/C > PtRuNiP_a/C > PtRuNiP-500/C > PtRuNiP-700/C, and the durability of PtRu/C catalyst is poorer than those of four PtRuNiP/C catalysts in terms of the specific activity.

Based on the above electrochemical results, the electrocatalytic performance of the four catalysts shows a regular volcano trend. As

Table 3
Electrochemical characterizations of the five catalysts.

Catalyst	The onset potential of methanol oxidation (V vs. RHE)	The specific activity at 0.797 V (mA cm ⁻²)	The mass activity at 0.797 V (mA mg ⁻¹ PtRu)
PtRuNiP _a /C	0.367	0.853	395
PtRuNiP-300/C	0.337	0.977	459
PtRuNiP-500/C	0.397	0.526	178
PtRuNiP-700/C	0.397	0.494	168
PtRu/C	0.451	0.874	418

mentioned before, the electrocatalytic characteristics including activity and durability are strongly affected by the surface atomic arrangement and configuration associated with terraces, steps, kinks, and vacancies [3,4]. Therefore, these four catalysts can firstly be divided into two categories in terms of the component of Ru species obtained from XPS: i) PtRuNiP_a/C and PtRuNiP-300/C, in which oxidized Ru is the major species; ii) PtRuNiP-500/C and PtRuNiP-700/C, where most of Ru species is metallic state. Moreover, the content of RuO_xH_y in PtRuNiP_a/C and PtRuNiP-300/C is up to ca. 18% (see Table 2); while RuO_xH_y isn't found in PtRuNiP-500/C and PtRuNiP-700/C. It is generally considered that the existence of oxidized Ru species on PtRu catalysts will result in enhanced electrocatalytic performance; these oxidized Ru species act as active centers for the generation of Ru–OH species which are essential in lowering potentials for the oxidative removal of CO-like poisoning intermediates from the surfaces of PtRu catalysts [25,38,54,55]. The superior performance of the RuO_xH_y-rich PtRu catalysts is attributed to the uniqueness of RuO_xH_y as a mixed electron/proton conductor innately related with a Ru–OH speciation [56]. The beneficial effect of RuO_xH_y on methanol electro-oxidation was thereafter frequently confirmed experimentally by several groups [57–59]. Based on these reports, it can be suggested that the existence of RuO_xH_y in PtRuNiP_a/C and PtRuNiP-300/C is one of the factors which lead to the high catalytic activity. Moreover, the ECSA of PtRuNiP_a/C and PtRuNiP-300/C are larger than those of PtRuNiP-500/C and PtRuNiP-700/C, which can also

improve the catalytic activity. In addition, based on XPS data, the bond strength of adsorbents towards small molecule for PtRuNiP_a/C and PtRuNiP-300/C is lower than PtRuNiP-500/C and PtRuNiP-700/C, which could result in high catalytic activity due to rapid removal of intermediates to recover the active sites [60].

On the other hand, for PtRuNiP_a/C and PtRuNiP-300/C, the surface composition and ECSA values are almost same, and the average particle size of PtRuNiP-300 nanoparticles is larger than that of PtRuNiP_a, but PtRuNiP-300/C exhibits higher catalytic activity than PtRuNiP_a/C. Why is this so? Because, as shown in Fig. 8, heat-treatment at 300 °C, annihilation of point defects and dislocation within the grains and grain boundary lead to the long-range disorder in PtRuNiP_a nanoparticles, along with the rearrangement of atoms. The changed range of disorder alters the electron state around atoms, which presents itself as the slightly positive shift of Pt 4f binding energy from PtRuNiP_a/C to PtRuNiP-300/C, implying the bond strength of adsorbates towards small molecules on PtRuNiP-300/C decreases compared to PtRuNiP_a/C, resulting in increased catalytic activity.

However, when the heat treatment temperature continually increase, the Pt 4f binding energy shifts to lower value, indicating that the bond strength of adsorbents towards small molecules increases which leads to low catalytic activity. Thus, the catalytic activity of PtRuNiP-500/C is higher than that of PtRuNiP-700/C. From the above results it can be concluded that in amorphous PtRuNiP nanoparticles, there is an optimum range of disorder which can be controlled by thermal treatment in order to achieve the highest catalytic activity.

4. Conclusions

In this study, the characterization results obtained using DSC, XRD, SAED, TEM, line-scan EDS and XPS have provided important information to explain the changes of long-range disorder, medium-range disorder and medium-range order as a function of the thermal treatment temperature. With the heat treatment temperature increase, the structure of PtRuNiP_a nanoparticles changed from long-range disorder to medium-range disorder, and the PtRuNiP nanoparticles became partial crystalline at 700 °C. CVs and chronoamperometry were carried out to study electrocatalytic performance. It was found that the catalytic activities as a function of the heat-treatment showed a volcanic curve trend and reached the peak when the heat treatment temperature was 300 °C which was caused by two factors, namely, the change of surface composition and the electronic effect which resulted from the changed range of disorder. The results are expected to pave the way for developing another strategy for developing amorphous multielemental nanoscale catalysts with high activity and durability for electrocatalytic reactions.

Acknowledgments

The authors acknowledge the National Natural Science Foundation of China (21363022, 21163018, and 51362027) for providing funding for this research.

Appendix A. Supplementary data

Supplementary data related to this article can be found at <http://dx.doi.org/10.1016/j.jpowsour.2014.06.091>.

References

- [1] L. Ma, C. Liu, J. Liao, T. Lu, W. Xing, J. Zhang, *Electrochim. Acta* 54 (2009) 7274–7279.

- [2] G. Wu, R. Swaidan, D. Li, N. Li, *Electrochim. Acta* 53 (2008) 7622–7629.
- [3] Z. Quan, Y. Wang, J. Fang, *Acc. Chem. Res.* 46 (2013) 191.
- [4] W.P. Zhou, A. Lewera, P.S. Bagus, A. Wieckowski, *J. Phys. Chem. C* 111 (2007) 13490–13496.
- [5] N. Tian, Z.-Y. Zhou, S.G. Sun, *J. Phys. Chem. C* 112 (2008) 19801–19817.
- [6] W. Chrzanoski, A. Wieckowski, *Langmuir* 13 (1997) 5974–5978.
- [7] S. Jones, K. Tedsree, M. Sawangphruk, J.S. Foord, J. Fisher, D. Thompson, S.C.E. Tsang, *ChemCatChem* 2 (2010) 1089–1095.
- [8] N. Tian, Z.-Y. Zhou, S.-G. Sun, Y. Ding, Z.L. Wang, *Science* 316 (2007) 732–735.
- [9] W.Y. Wong, W.R.W. Daud, A.B. Mohamad, A.A.H. Kadhum, K.S. Loh, E.H. Majlan, *Int. J. Hydrogen Energy* 38 (2013) 9370–9386.
- [10] K. Asami, A. Kawashima, A. Hashimoto, *Mater. Sci. Eng.* 99 (1998) 475.
- [11] K. Wang, H. Wang, R. Wang, J. Key, V. Linkov, S. Ji, S. Afr. J. Chem. 66 (2013) 86–91.
- [12] T.F. Hung, M.H. Tu, C.W. Tsai, C.J. Chen, R.S. Liu, W.R. Liu, M.Y. Lo, *Int. J. Hydrogen Energy* 38 (2013) 3956–3962.
- [13] M. Muraoka, H. Tomonaga, M. Nagai, *Fuel* 97 (2012) 211–218.
- [14] J. Barranco, A.R. Pierna, J.R. Non-Cryst. Solids 353 (2007) 851–854.
- [15] G. Yang, Y. Chen, Y. Zhou, Y. Tang, T. Lu, *Electrochem. Commun.* 12 (2010) 492–495.
- [16] X. Xue, J. Ge, T. Tian, C. Liu, W. Xing, T. Lu, *J. Power Sources* 172 (2007) 560–569.
- [17] X. Xue, J. Ge, C. Liu, W. Xing, T. Lu, *J. Electrochem. Commun.* 8 (2006) 1280–1286.
- [18] M.L. Lin, M.Y. Lo, C.Y. Mou, *Catal. Today* 160 (2011) 109–115.
- [19] H. Daimon, Y. Kurobe, *Catal. Today* 111 (2006) 182–187.
- [20] L.X. Ding, A.L. Wang, G.R. Li, Z.Q. Liu, W.X. Zhao, C.Y. Su, Y.X. Tong, *J. Am. Chem. Soc.* 134 (2012) 5730–5733.
- [21] S.H. Lee, D.J. Kim, Y.S. Yoon, *Jpn. J. Appl. Phys.* 52 (2013) 035001.
- [22] C. Massobrio, A. Pasquarello, *Phys. Rev. B* 77 (2008) 144207–144216.
- [23] J.N. Balaraju, Kalavati, N.T. Manikandanath, V.K. William Grips, *Surf. Coat. Technol.* 206 (2012) 2682–2689.
- [24] H. Huang, H. Chen, D. Sun, X. Wang, *J. Power Sources* 204 (2012) 46–52.
- [25] Y.C. Wei, C.W. Liu, W.J. Chang, K.W. Wang, *J. Alloys Compd.* 509 (2011) 535–541.
- [26] S.Y. Huang, S.M. Chang, C.L. Lin, C.H. Chen, C.T. Yeh, *J. Phys. Chem. B* 110 (2006) 23300–23305.
- [27] W. Wang, Y. Li, H. Wang, *Reac. Kinet. Mech. Cat.* 108 (2013) 433–441.
- [28] H. Wang, X. Zhang, R. Wang, S. Ji, W. Wang, Q. Wang, Z. Lei, *J. Power Sources* 196 (2011) 8000–8003.
- [29] H. Wang, S. Ji, W. Wang, R. Wang, S. Afr. J. Chem. 66 (2013) 17–20.
- [30] H. Li, J. Liao, X. Zhang, W. Liao, L. Wen, J. Yang, H. Wang, R. Wang, *J. Power Sources* 239 (2013) 277–283.
- [31] H.W. Sheng, W.K. Luo, F.M. Alamgir, J.M. Bai, E. Ma, *Nature* 439 (2006) 419–425.
- [32] T.C. Hufnagel, *Nat. Mater.* 3 (2004) 666–667.
- [33] H. Peng, Z. Mo, S. Liao, H. Liang, L. Yang, F. Luo, H. Song, Y. Zhong, B. Zhang, *Sci. Rep.* 3 (2013) 1765.
- [34] X.L. Wang, H. Wang, Z.Q. Lei, Z. Zhang, R.F. Wang, *Chin. J. Catal.* 32 (2011) 1519–1524.
- [35] B.N. Wanjala, J. Luo, R. Loukrakpam, B. Fang, D. Mott, P.N. Njoki, M. Engelhard, H.R. Naslund, J.K. Wu, L. Wang, O. Malis, C.J. Zhong, *Chem. Mater.* 22 (2010) 4282–4294.
- [36] L. Xu, G. Zhang, J. Chen, Y. Zhou, G.e. Yuan, F. Yang, *J. Power Sources* 240 (2013) 101–108.
- [37] L. Wei, Y.-J. Fan, J.-H. Ma, L.-H. Tao, R.-X. Wang, J.-P. Zhong, H. Wang, *J. Power Sources* 238 (2013) 157–164.
- [38] S.Y. Huang, C.M. Chang, K.W. Wang, C.T. Yeh, *ChemPhysChem* 8 (2007) 1774–1777.
- [39] Y.C. Wei, C.W. Liu, K.W. Wang, *ChemPhysChem* 10 (2009) 1230–1237.
- [40] J.L. Gómez de la Fuente, M.V. Martínez-Huerta, S. Rojas, P. Hernández-Fernández, P. Terreros, J.L.G. Fierro, M.A. Peña, *Appl. Catal. B* 88 (2009) 505–514.
- [41] Y. Liang, J. Li, Q.-C. Xu, R.-Z. Hu, J.-D. Lin, D.-W. Liao, *J. Alloys Compd.* 465 (2008) 296–304.
- [42] M. Cini, M. De Crescenzi, F. Patella, N. Motta, M. Sastry, F. Rochet, R. Pasquali, A. Balzarotti, C. Verdozzi, *Phys. Rev. B* 41 (1990) 5685–5695.
- [43] M.G. Mason, *Phys. Rev. B* 27 (1983) 748–762.
- [44] G.K. Wertheim, S.B. DiCenzo, D.N.E. Buchanan, *Phys. Rev. B* 33 (1986) 5384–5390.
- [45] B. Richter, H. Kühlenbeck, H.J. Freund, P. Bagus, *Phys. Rev. Lett.* 93 (2004) 026805.
- [46] W.P. Zhou, A. Lewera, R. Larsen, R.I. Masel, P.S. Bagus, A. Wieckowski, *J. Phys. Chem. B* 110 (2006) 13393–13398.
- [47] X. Zhang, H. Wang, J. Key, V. Linkov, S. Ji, X. Wang, Z. Lei, R. Wang, *J. Electrochem. Soc.* 159 (2012) B270–B276.
- [48] J. Prabhuram, T.S. Zhao, Z.K. Tang, R. Chen, Z.X. Liang, *J. Phys. Chem. B* 110 (2006) 5245–5252.
- [49] P. Hernandez-Fernandez, R. Nuno, E. Fatas, J.L.G. Fierro, P. Ocon, *Int. J. Hydrogen Energy* 36 (2011) 8267–8278.
- [50] L.P.R. Profeti, D. Profeti, P. Olivi, *Int. J. Hydrogen Energy* 34 (2009) 2747–2757.
- [51] H.A. Gasteiger, N. Markovic, P.N. Ross, E.J. Cairns, *J. Phys. Chem.* 97 (1993) 12020–12029.

- [52] C. Zhou, H. Wang, F. Peng, J. Liang, H. Yu, J. Yang, *Langmuir* 25 (2009) 7711–7717.
- [53] H. Li, D.L. Kang, H. Wang, R.F. Wang, *Int. J. Electrochem. Sci.* 6 (2011) 1058–1065.
- [54] H.B. Suffredini, V. Tricoli, N. Vattistas, L.A. Avaca, *J. Power Sources* 158 (2006) 124–128.
- [55] S.Y. Huang, C.T. Yeh, *J. Power Sources* 195 (2010) 2638–2643.
- [56] D.R. Rolison, P.L. Hagans, K.E. Swider, J.W. Long, *Langmuir* 15 (1999) 774–779.
- [57] S. Zhu, S. Wang, Y. Gao, L. Jiang, H. Sun, G. Sun, *Int. J. Hydrogen Energy* 35 (2010) 11254–11260.
- [58] J.H. Ma, Y.Y. Feng, J. Yu, D. Zhao, A.-J. Wang, B.Q. Xu, *J. Catal.* 275 (2010) 34–44.
- [59] B. Shyam, T.M. Arruda, S. Mukerjee, D.E. Ramaker, *J. Phys. Chem. C* 113 (2009) 19713–19721.
- [60] X. Mao, L. Yang, J. Yang, J. Key, S. Ji, H. Wang, R. Wang, *J. Electrochem. Soc.* 160 (2013) H219–H223.